



1 **Effect of normal stress on the friction of brucite:**  
2 **Application to slow earthquake in the mantle wedge**

3 Hanaya Okuda<sup>1,2</sup>, Ikuo Katayama<sup>3</sup>, Hiroshi Sakuma<sup>4</sup>, Kenji Kawai<sup>1</sup>

4

5 <sup>1</sup>Department of Earth and Planetary Science, School of Science, University of Tokyo, Bunkyo, 113-0033  
6 Tokyo, Japan

7 <sup>2</sup>Department of Ocean Floor Geoscience, Atmosphere and Ocean Research Institute, University of Tokyo,  
8 Kashiwa, 277-8564 Chiba, Japan

9 <sup>3</sup>Department of Earth and Planetary Systems Science, Hiroshima University, Higashi-Hiroshima, 739-8526  
10 Hiroshima, Japan

11 <sup>4</sup>Research Center for Functional Materials, National Institute for Materials Science, Tsukuba, 305-0044  
12 Ibaraki, Japan

13

14 *Correspondence to:* Hanaya Okuda (okuda@aori.u-tokyo.ac.jp)

15



16 **Abstract**

17           We report the results of friction experiments on brucite under both dry and water-saturated (wet)  
18 conditions under various normal stresses (10–60 MPa). The steady-state friction coefficients of brucite were  
19 determined to be 0.40 and 0.26 for the dry and wet cases, respectively, independent of the normal stress.  
20 Under dry conditions, velocity-weakening behavior was observed in all experiments at various normal  
21 stresses. Under wet conditions, velocity weakening was observed at low normal stress (10 and 20 MPa),  
22 whereas velocity strengthening was determined at a higher applied normal stress. The microstructural  
23 observations on recovered experimental samples indicate localized deformation within the narrow shear  
24 band, implying that a small volume of brucite can control the bulk strength in an ultramafic setting and  
25 significantly change the frictional properties. Brucite is found to be the only mineral that has a low friction  
26 coefficient and exhibits unstable frictional behavior under hydrated mantle wedge conditions, explaining  
27 the occurrence of slow earthquakes in the mantle wedge.

28



## 29 **1. Introduction**

30           Serpentinite is generated by the hydration of ultramafic rocks and has various mineral  
31 compositions depending on temperature–pressure conditions of the MgO–SiO<sub>2</sub>–H<sub>2</sub>O system (Evans et al.,  
32 2013). As serpentinite has been observed in various important tectonic settings and is considered to  
33 contribute to the weakness of serpentinite-dominant areas, the frictional properties of serpentinite have been  
34 investigated for several decades (see Guillot et al., 2015; Hirth and Guillot, 2013 for a review). A large  
35 volume of serpentinite is located in the mantle wedge in which olivine-rich rock of the upper mantle is  
36 hydrated due by slab-derived water and its mechanical weakness could contribute to the aseismic behavior  
37 below the downdip limit of seismogenic zones (Hyndman and Peacock, 2003; Oleskevich et al., 1999).

38           The mantle wedge is mainly composed of an antigorite–olivine assemblage in the case of warm  
39 subduction zones like Cascadia, whereas a brucite–antigorite assemblage dominates in the case of cold  
40 subduction zones such as that in NE Japan (Peacock and Hyndman, 1999). Because fluids from subducting  
41 slabs have a high SiO<sub>2</sub> content, talc is stable in the vicinity of slab–mantle boundaries (Hirauchi et al., 2013;  
42 Peacock and Hyndman, 1999). The mineral composition of serpentinite has a strong effect on the  
43 mechanical behavior of bulk serpentinite because each serpentinite-related mineral, such as antigorite,  
44 brucite, and talc, has a different frictional behavior. Despite a variety of previous experimental  
45 investigations of the frictional properties of antigorite and talc (Hirauchi et al., 2013; Moore et al., 1997;  
46 Moore and Lockner, 2007, 2008; Okazaki and Katayama, 2015; Reinen et al., 1994; Sánchez-Roa et al.,  
47 2017; Takahashi et al., 2007; Tesei et al., 2018), brucite has rarely been considered in previous studies  
48 compared with other serpentinite-related minerals, which might be due to the fact that it is difficult to detect  
49 brucite under natural conditions because of its fine-grained nature (Hostetler et al., 1966). Recent geological  
50 work on the paleo-mantle wedge in SW Japan revealed the presence of brucite and suggested that silica  
51 metamorphism has not widely occurred within the shallow mantle wedge (Kawahara et al., 2016; Mizukami  
52 et al., 2014). In addition, brucite was also detected in ultramafic clasts that erupted from mud volcanoes of



53 the Mariana forearc mantle where the cold Mariana Plate subducts beneath the Philippine Sea Plate  
54 (D'Antonio and Kristensen, 2004). Because brucite is stable in the mantle wedge, its frictional properties  
55 should be investigated to understand the seismic activities in hydrated mantle wedges.

56           Only a few previous experimental studies have been conducted on the frictional properties of  
57 brucite. It was shown that brucite has friction coefficients of 0.40–0.46 (dry) or 0.28 (wet), which are lower  
58 than those of antigorite (Moore and Lockner, 2004, 2007; Morrow et al., 2000). Regarding the velocity  
59 dependence, stick-slip behavior is significant for dry brucite at both room and high temperature, implying  
60 velocity weakening. Conversely, wet brucite shows velocity-strengthening behavior at room temperature,  
61 which gradually changes to velocity weakening with increasing temperature (Moore et al., 2001; Moore  
62 and Lockner, 2007). Because the friction coefficient of the serpentinite gouge can be lowered by about  
63 ~10–15 % due to the presence of brucite (Moore et al., 2001) in addition to velocity-weakening behavior  
64 of brucite under certain conditions, the frictional characteristics of brucite might affect earthquake  
65 nucleation processes at mantle wedges. Although the mantle wedge is generally close to the downdip limit  
66 of seismogenic zones (Hyndman and Peacock, 2003; Oleskevich et al., 1999), many recent observations  
67 indicated slow earthquakes at the depth of the mantle wedge in various subduction zones (Audet and Kim,  
68 2016; Obara and Kato, 2016). Therefore, the weak, unstable frictional behavior of brucite might be the key  
69 to understand the occurrence of slow earthquakes at mantle wedges.

70           The effective normal stress is an important parameter that constrains the frictional behavior  
71 because the apparent frictional strength of a material decreases with decreasing effective normal stress.  
72 Near lithostatic pore pressure conditions, which leads to low effective normal stress conditions, have been  
73 inferred based on seismic velocity structures at the plate interfaces of several subduction zones where slow  
74 earthquakes coincidentally occur such as Cascadia, SW Japan, Central Mexico, and Hikurangi (Audet et  
75 al., 2009; Audet and Kim, 2016; Eberhart-Phillips and Reyners, 2012; Matsubara et al., 2009; Shelly et al.,  
76 2006; Song and Kim, 2012). Importantly, low effective normal stress is favorable for the nucleation of slow



77 earthquake (Liu and Rice, 2007, 2009; Rubin, 2008; Segall et al., 2010). Although the frictional behavior  
78 of brucite at low effective normal stress could be directly related to the occurrence of slow earthquake in  
79 the mantle wedge, previous studies have been conducted at high effective normal stresses of 100 or 150  
80 MPa (Moore et al., 2001; Moore and Lockner, 2007) but not at low effective normal stress. In this study,  
81 we experimentally investigated the frictional behavior of brucite at various effective normal stresses  
82 ranging from 10 to 60 MPa to understand the effect of brucite on the seismic activities in hydrated mantle  
83 wedges. Because brucite shows a weak and unstable frictional behavior under a wide range of pressure–  
84 temperature conditions, it is a key material controlling the nucleation of earthquakes in hydrated mantle  
85 wedges.

86

## 87 **2. Methods**

### 88 **2.1. Friction experiment**

#### 89 **2.1.1. Sample preparation**

90 Brucite nanoparticles with a grain size of 70 nm chemically synthesized by WAKO were used  
91 for the friction experiments to simulate its fine-grained nature (Fig. 1). The synthetic samples had a purity  
92 of 99.9 % (data from WAKO).

93 A biaxial testing machine at Hiroshima University, Japan, was used for all friction experiments  
94 in this study (Noda and Shimamoto, 2009). Two gouge layers were formed with three gabbro blocks (Fig.  
95 1). The surfaces in contact with gouges were roughened before the experiments using Carborundum (grit  
96 80) to prevent slip between the block and sample. All brucite samples were dried in the vacuum oven  
97 overnight under 120 °C before the experiments. This temperature was selected to remove adsorbed water  
98 and prevent the dehydroxylation of brucite into periclase (MgO). For the dry experiments, the brucite  
99 powder was quickly placed in each of the two gouges after removing it from the vacuum oven and blocks



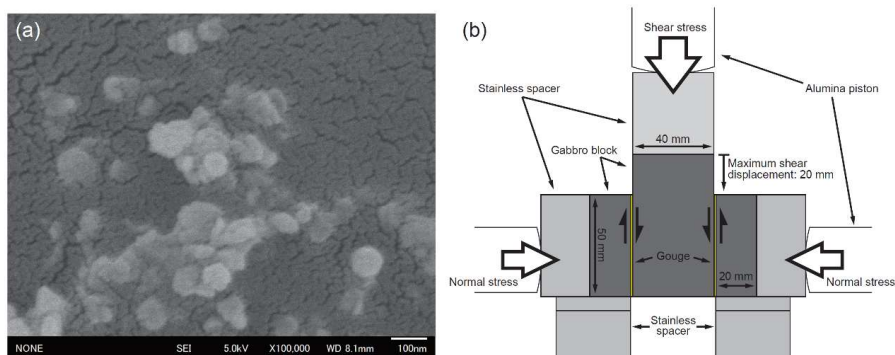
100 were put in the testing machine. For the wet experiments, dried brucite was mixed with distilled water until  
101 saturation before placing it in the gouges and then sandwiched between blocks.

102

### 103 2.1.2. Experimental procedures

104 Normal stress was horizontally applied on the side blocks, and shear stress was applied vertically  
105 by pushing the center block downward (Fig. 1). Before applying shear stress, the desired normal stress was  
106 applied to the blocks for 1 h to prevent an effect of the compaction of the gouge during shear deformation  
107 (nominally precompaction). For the wet experiments, the blocks and gouges were placed in the tank filled  
108 with distilled water for 1 h under a normal stress of 250 kPa before the precompaction with the desired  
109 normal stress such that water-saturated conditions were achieved. After the precompaction, shear stress was  
110 applied with a constant load point velocity of  $3 \mu\text{m s}^{-1}$ . Velocity step tests were repeatedly conducted after  
111 the shear displacement reached 10 mm by abruptly increasing the load point velocity to  $33 \mu\text{m s}^{-1}$  and  
112 decreasing it to  $3 \mu\text{m s}^{-1}$  after sliding of 1 mm (Fig. 2). The normal stress conditions of 10, 20, 40, and 60  
113 MPa were tested for both the dry and wet cases to study the influence of effective normal stress. In addition,  
114 several experiments were conducted with different shear displacements to investigate the evolution of the  
115 gouge microstructure in both the dry and wet experiments (Table 1).

116



117



118 **Figure 1: (a) SEM micrograph of synthetic brucite used in this study. The scale bar is 100 nm. (b) Schematic**  
119 **view of the biaxial testing machine used in this study.**

120

121

## 122 **2.2. Data analysis**

### 123 **2.2.1. Mechanical data**

124 The friction coefficient  $\mu$  was calculated from the ratio of the shear stress to the normal stress.  
125 Note that cohesion was not considered because the cohesion stresses were 0.36 and 0.47 MPa for the dry  
126 and wet cases, respectively, which are much smaller than the tested normal stress conditions. The shear  
127 displacement was corrected using the stiffness of the testing machine ( $4.4 \times 10^8 \text{ N m}^{-1}$ ). The velocity step  
128 tests were analyzed using the rate- and state-dependent friction (RSF) law (Dieterich, 1979; Ruina, 1983).  
129 The slip dependency, which was calculated from the later part of each velocity step test with a shear  
130 displacement of 500  $\mu\text{m}$ , was detrended before conducting the following analyses. Detrended data were  
131 fitted to the following the RSF law:

$$132 \quad \mu = \mu_0 + a \ln\left(\frac{V}{V_0}\right) + b_1 \ln\left(\frac{V_0 \theta_1}{d_{c1}}\right) + b_2 \ln\left(\frac{V_0 \theta_2}{d_{c2}}\right), \quad (1)$$

133 where  $a$ ,  $b_1$  and  $b_2$  are nondimensional parameters,  $\mu_0$  is the steady-state friction coefficient before the  
134 velocity step,  $V_0$  and  $V$  are the sliding velocities before and after the velocity step,  $d_{c1}$  and  $d_{c2}$  are the  
135 characteristic slip distances, and  $\theta_1$  and  $\theta_2$  are the state variables. The transition of  $V$  was calculated by  
136 the following relationship:

$$137 \quad \frac{d\mu}{dt} = k(V_{lp} - V), \quad (2)$$

138 where  $V_{lp}$  is the load point velocity, which was abruptly changed, and  $k$  is the system stiffness, which was  
139 treated as an unknown parameter (in  $\mu\text{m}^{-1}$ ). The Dieterich (aging) law (Dieterich, 1979; Marone, 1998;  
140 Ruina, 1983) was used for the state variable in this study.



141 
$$\frac{d\theta_i}{dt} = 1 - \frac{V\theta_i}{d_{ci}}, i = 1, 2 \quad (3)$$

142 A MATLAB code, RSFit3000, developed to fit the velocity step and slide hold slide tests (Skarbek and  
143 Savage, 2019) was used for the analyses of velocity step tests. Second variables  $b_2$ ,  $\theta_2$  and  $d_{c2}$  (Blanpied  
144 et al., 1998) were only introduced when the experimental data were poorly fitted (upsteps of HTB575 and  
145 HTB598; Fig. 4); otherwise,  $b_2$  and  $\theta_2$  were treated as 0. The value of  $a - b$  ( $a - b_1 - b_2$ , or  $a - b_1$ )  
146 was then calculated for each step, which describes the instability of the simulated fault: the state of fault is  
147 defined as velocity strengthening and stable when  $a - b$  is positive, whereas it is defined as velocity  
148 weakening and potentially unstable when  $a - b$  is negative. Note that  $d_c$  for the downsteps is larger than  
149 that for the upsteps. Because we chose to use the Dieterich (aging) law to fit the RSF law,  $d_c$  reflects the  
150 contact diameter of the asperity contact (Dieterich, 1979; Ruina, 1983). When the load point velocity is 3  
151  $\mu\text{m s}^{-1}$ , the lifetime of one asperity contact becomes longer than that with a load point velocity of 33  $\mu\text{m s}^{-1}$ .  
152 Therefore, the contact diameter,  $d_c$ , for the load point velocity of 3  $\mu\text{m sec}^{-1}$  (downsteps) becomes larger  
153 than that for 33  $\mu\text{m s}^{-1}$  (upsteps). Although there are still debates on the choice of constitutive laws  
154 (Bhattacharya et al., 2015, 2017; Marone, 1998), the value of  $a - b$  is more critical for seismic activities.

155 When the system is velocity weakening, that is,  $a - b$  is negative, it starts to vibrate  
156 automatically (stick-slip) when the system stiffness is lower than the critical stiffness, whereas conditionally  
157 stable sliding is achieved when the system stiffness is higher than the critical stiffness. The critical stiffness  
158  $k_c$  can be described as follows when quasi-static stick-slip behavior is assumed:

159 
$$k_c = \frac{N(b - a)}{d_c}, \quad (4)$$

160 where  $N$  is the applied normal force (Ruina, 1983). Thus, as the normal force  $N$  applied to the velocity-  
161 weakening system increases, the system starts to show stick-slip behavior. In other words, the occurrence  
162 of stick-slip represents that the system is velocity-weakening.

163





164 **2.2.2. Microstructure**

165           In the case of sheet-structure minerals, the friction between basal planes of the crystals [(0001)  
166 plane for brucite] is thought to be significant due to their weak bonding. The shear surfaces of the samples  
167 recovered from friction experiments using sheet-structure minerals often show smooth surfaces based on  
168 platy particles aligned parallel to the sliding direction (Moore and Lockner, 2004). Under natural conditions,  
169 the aligned platy particles of interconnected talc were reported to contribute to low friction coefficient of  
170 the low angle normal fault (Collettini et al., 2009). The experimentally determined friction coefficients of  
171 single-crystalline muscovite and chlorite are much smaller than those of powdered polycrystalline samples  
172 (Horn and Deere, 1962; Kawai et al., 2015; Niemeijer, 2018; Okamoto et al., 2019).

173           Because these experiments indicate that the crystal orientation within the gouge has a significant  
174 effect on the friction coefficients of sheet-structure minerals, observations of thin sections of recovered  
175 samples were conducted after the experiments (Table 1) to investigate the effects of the deformation  
176 structures and crystal orientation within the gouges on the frictional behaviors. Thin sections parallel to the  
177 shear direction and normal to the gouges with a thickness of 30  $\mu\text{m}$  were prepared. The scanning electron  
178 microscope (SEM, JEOL JXA-8900 at the Atmosphere and Ocean Research Institute, University of Tokyo,  
179 Japan) was used for the observation of the microstructures of the gouges. An accelerating voltage of 15 kV  
180 and beam current of 10.0 nA were used for all backscattered electron (BSE) observations. The crystal  
181 orientation was determined with a polarizing microscope at the University of Tokyo, Japan.

182



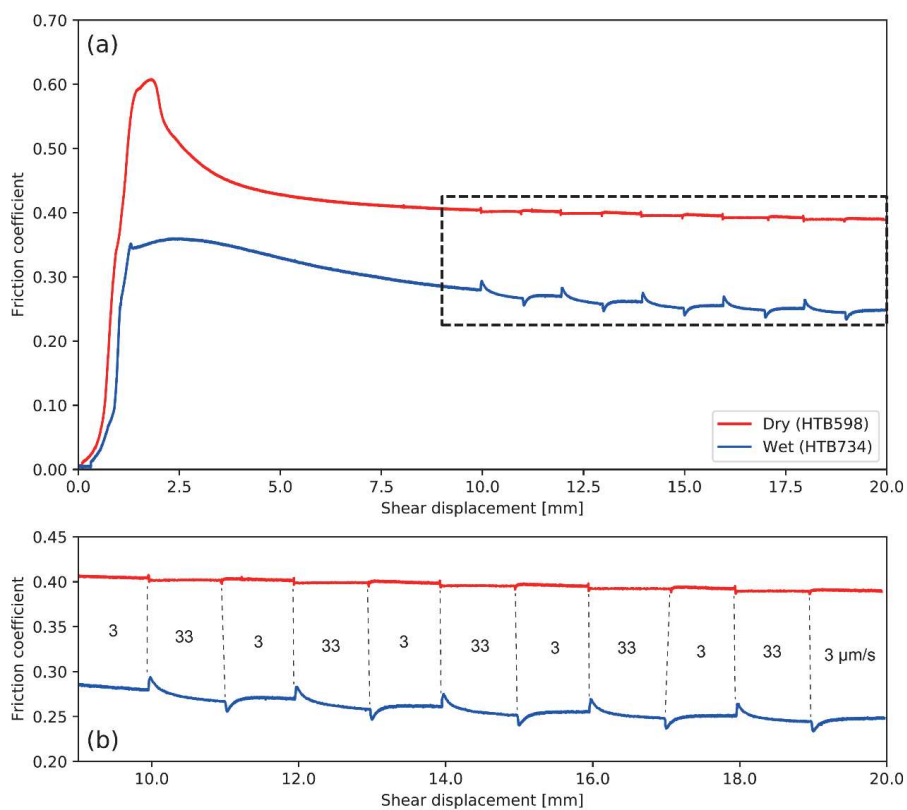
183 **3. Results**

184 **3.1. Mechanical behaviors**

185 **3.1.1. Friction coefficients**

186 In general, both dry and wet experiments initially show high friction coefficients (hereafter peak  
187 friction coefficients) followed by slip-weakening trends lasting about 10 mm shear displacement toward  
188 the steady state (Figs. 2 and S1). The steady state friction coefficients at a shear displacement of ~20 mm  
189 for dry and wet conditions under all normal stress conditions were 0.40(4) and 0.26(3), respectively (Table  
190 1). These steady-state friction coefficients are mostly independent of the applied normal stress (Fig. 3) and  
191 consistent with previous experimental results, that is, 0.38-0.46 and 0.28 for dry and wet brucite at an  
192 applied normal stress of 100 MPa at room temperature, respectively (Moore and Lockner, 2004, 2007). The  
193 friction coefficient for dry experiment is also close to the theoretical value of 0.30(3) (Okuda et al., 2019).  
194 Note that the peak friction coefficient of wet brucite at an effective normal stress of 60 MPa is high because  
195 of sudden stress drops in the initial stage of the shear displacement (Fig. S1).

196



197

198

199 **Figure 2: (a) Friction coefficients for dry (HTB598) and wet (HTB734) experiments at a normal stress of 20 MPa.**

200 **Slip-weakening behavior was observed after the peak under both dry and wet conditions. (b) Enhanced view of**

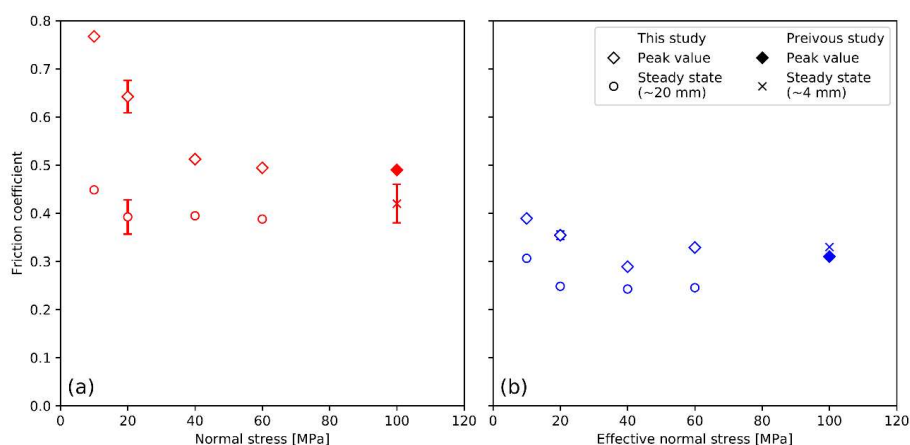
201 **velocity step sequences as indicated by the dotted square in (a). The velocities at given shear displacements are**

202 **displayed between two lines.**

203

204

205



206

207 **Figure 3: Relationship between normal stress and the peak or steady-state friction coefficients for the dry (a)**  
208 **and wet (b) experiments. Data at a normal stress of 100 MPa were obtained from previous experiments (Moore**  
209 **et al., 2001; Moore and Lockner, 2004, 2007; Morrow et al., 2000). The steady-state friction coefficients**  
210 **insignificantly depend on the applied normal stresses. For this study, the error bar represents the one-sigma**  
211 **standard deviation among multiple data. For 100 MPa dry data, the steady state value and the error bar denote**  
212 **the averaged value of stick-slip behavior and its amplitude, respectively. Note that the peak friction coefficient**  
213 **of wet brucite at an effective normal stress of 60 MPa is high because of sudden stress drops in the initial stage**  
214 **of the shear displacement (Fig. S1).**

215

216

### 217 3.1.2. Velocity dependencies

218 For wet experiments, negative  $a - b$  values were observed at low normal stresses of 10 and 20  
219 MPa (Figs. 4a and b). However, the  $a - b$  values became almost neutral at 40 MPa and positive at 60 MPa.  
220 A positive  $a - b$  value was consistent with the previous experiments on wet brucite at an effective normal  
221 stress of 100 MPa (Moore et al., 2001; Moore and Lockner, 2007). The  $a - b$  values obtained for the  
222 upsteps and downsteps insignificantly differ (Figs. 4a and b), which implies that the normal stress condition  
223 mainly controls the  $a - b$  values. The constitutive parameter  $a$  insignificantly depends on the applied  
224 normal stress, whereas  $b$  decreases as the normal stress increases, leading to the transition from negative



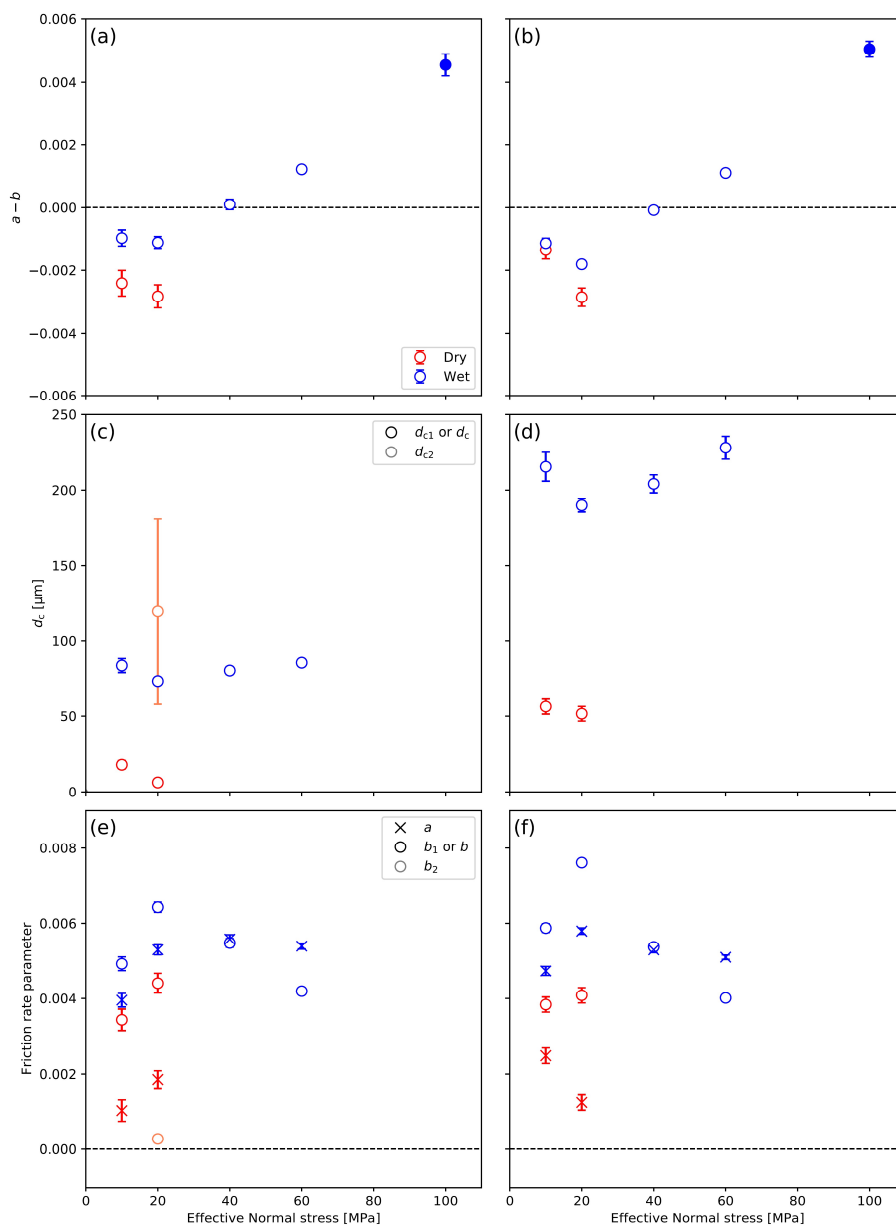
225 to positive  $a - b$  values (Figs. 4e and f). The  $d_c$  values at different effective normal stresses  
226 insignificantly differ (Figs. 4c and d).

227 For dry experiments, negative  $a - b$  values were obtained at normal stresses of 10 and 20 MPa  
228 (Figs. 4a and b). When the normal stress was higher than 40 MPa, stick-slip behavior was observed, which  
229 implies a negative sign of  $a - b$ . This unstable stick-slip behavior was also observed in the case of the dry  
230 experiment at a higher normal stress of 100 MPa (Moore and Lockner, 2004; Morrow et al., 2000). As  
231 shown in the wet conditions, larger  $d_c$  values were observed for the downsteps (Figs. 4c and d). Although  
232 the second variables  $b_2$  and  $d_{c2}$  were introduced in certain experiments (HTB575 and HTB598), their  
233 effects on the frictional characteristics are small because the  $b_2$  values are much smaller than  $b_1$  (Fig. 4e  
234 and Table S1).

235 The constitutive parameters  $a$  and  $b$  and critical slip distance  $d_c$  of the dry and wet  
236 experiments significantly differ. The  $a$ ,  $b$ , and  $d_c$  values of the wet experiments are larger than those of  
237 the dry experiments (Fig. 4). The critical slip distances  $d_c$  of the upsteps and downsteps under wet  
238 conditions were 5–15 times and 3–4 times larger than those under dry conditions, respectively.

239

240



241  
 242 **Figure 4: Results of the velocity step tests. Values of  $a - b$  for upsteps (a) and downsteps (b),  $d_c$  for upsteps**  
 243 **(c) and for downsteps (d),  $a$  and  $b$  for upsteps (e) and for downsteps (f). The errors represent the one-sigma**  
 244 **standard deviations of all upsteps or downsteps under each experimental condition including the errors of the**  
 245 **nonlinear least square fitting processes. The  $a - b$  values at a normal stress of 100 MPa were obtained from a**



246 previous study (solid symbol; Moore et al., 2001). Because stick-slip behavior was observed in the dry  
247 experiments at normal stresses of 40, 60, and 100 MPa, negative values of  $a - b$  are expected; however, exact  
248 values could not be estimated (Sect. 3.1.2). Second variables  $b_2$  and  $d_{c2}$  were introduced for upsteps of the dry  
249 experiments at a normal stress of 20 MPa.

250

### 251 3.2. Microstructure

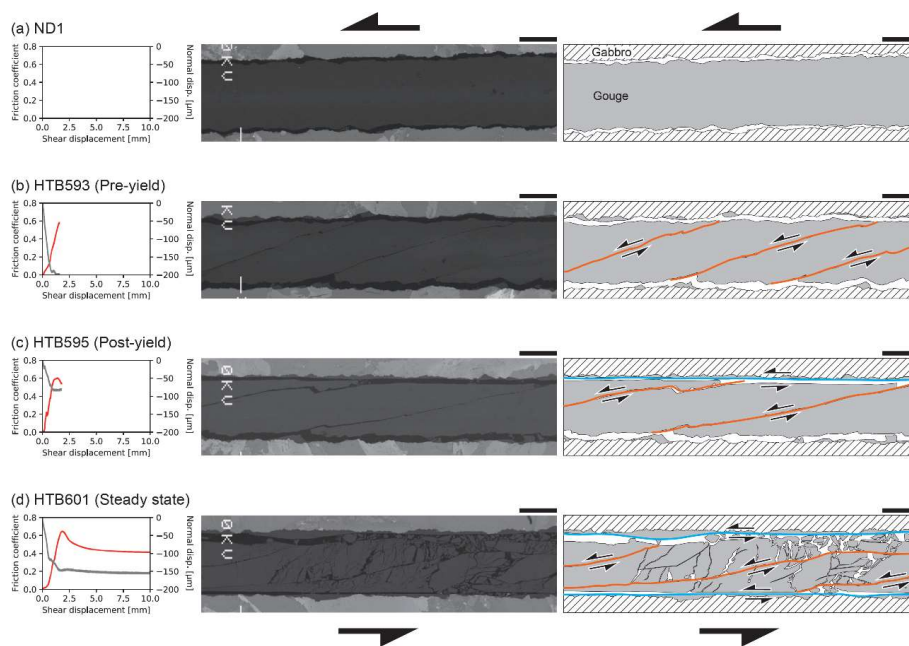
#### 252 3.2.1. Evolution of deformation structures

253 As all samples (both dry and wet) showed peak and steady states, we chose shear displacements  
254 before the peak friction coefficient (pre-yield), after the peak friction coefficient (post-yield), and in the  
255 steady state (10 mm). We followed the description of the microstructure of a sheared gouge by Logan et al.  
256 (1979). The results for the dry and wet experiments are shown in Figs. 5 and 6, respectively.

257 Before the shear loading, no shear structure was observed (Fig. 5a). When the shear force was  
258 loaded, the Riedel shear propagated in the pre-yield regime and the gouge width shortened rapidly at first  
259 (Figs. 5b and 6a). Subsequently, the boundary shear started to develop in the post-yield (Figs. 5c and 6b).  
260 In the steady state, the boundary shear was created by the gouge and the Riedel shear tilted subparallel to  
261 the boundary shear (Figs. 5d and 6c). The surfaces of the gabbro blocks were filled with brucite and the  
262 boundary shear was much smoother than the original block surface. These observations are consistent with  
263 those of previous studies (Haines et al., 2013; Logan et al., 1992; Marone, 1998), although clear Y shear  
264 and P foliation were not observed in this study. The gouge width remained almost constant following the  
265 post-yield and in the steady state. The width of the entire gouge in the steady state was 400 and 150  $\mu\text{m}$  in  
266 the dry and wet cases, respectively (Figs. 5d and 6c). The narrow width of the gouge in the wet case may  
267 be the result of the leaking the sample during the experiment, although the deformation processes of the  
268 dry and wet cases do not differ, as shown above.

269

270



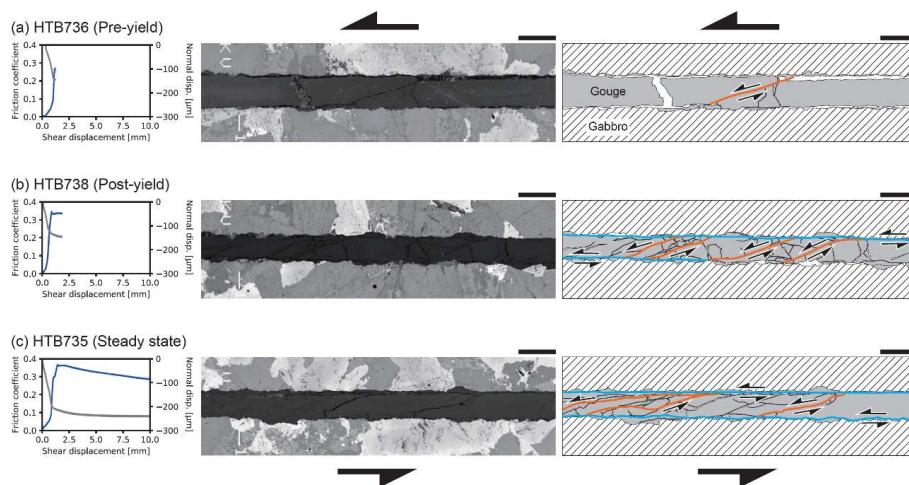
271  
 272 **Figure 5: Backscattered electron (BSE) images showing the deformation of gouges (center) and corresponding**  
 273 **interpretive sketches (right) of the dry experiments. The friction coefficients and normal displacement are shown**  
 274 **in the left panels using colored and gray lines. The orange lines, blue lines, gray area, hatched area, and white**  
 275 **area in the sketches correspond to the Riedel shear, boundary shear, brucite gouge, gabbro block, and epoxy**  
 276 **resin, respectively. The arrows represent the slip directions. The scale bars represent 200  $\mu\text{m}$ .**

277

278

279





280

281 **Figure 6: Backscattered electron (BSE) images showing the deformation of gouges (center) and corresponding**  
282 **interpretive sketches (right) of the wet experiments. See Fig. 6 for descriptions.**

283

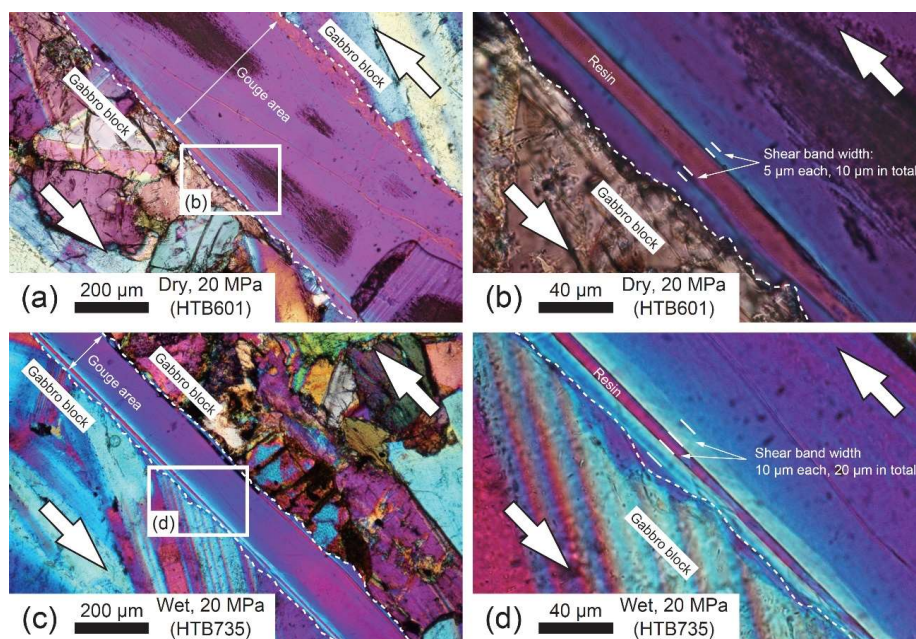
### 284 3.2.2. Crystal orientation

285 Because the elongation of brucite is length fast (Berman, 1932) and its birefringence is 0.014–  
286 0.020 (Deer et al., 2013), the interference color of brucite under crossed nicols with the sensitive color plate  
287 inserted becomes second-order blue or first-order yellow when the  $c$  axis of brucite is normal or parallel to  
288 the  $X'$ -direction of the sensitive color plate, respectively.

289 In the dry sample (HTB601; Figs. 7a and 7b), a second-order blue line can be observed parallel  
290 to the smooth boundary shear. This implies that the basal (0001) plane of the brucite particles is aligned  
291 along the boundary shear parallel to the shear direction. Based on the magnified view, the brucite particles  
292 are oriented within 10  $\mu\text{m}$  around the boundary shear (Fig. 7b). Because the purple area indicates that the  
293 brucite particles are randomly oriented, the shear strain can be localized within a width of 10  $\mu\text{m}$ . Hereafter,  
294 we call this oriented area “shear band.” In the wet samples, the crystals are also oriented along the boundary  
295 shear (Figs. 7c and 7d). The width of the shear band is 20  $\mu\text{m}$  (Fig. 7d), that is, the same as in the dry case.



296 Note that detailed transmission electron microscopy is required in future studies to confirm the crystal  
297 orientation and shear band width, similar to previous studies (Verberne et al., 2014a; Viti, 2011).  
298



299  
300 **Figure 7: Observation of the crystal orientation using the polarizing microscope under crossed nicols with the**  
301 **sensitive color plate. The arrows indicate the shear direction. The X'-direction of the sensitive color plate is**  
302 **parallel to the shear direction. (a) Dry experiment with 20 MPa normal stress (HTB601). (c) Wet experiment**  
303 **with 20 MPa normal stress (HTB735). (b and d) Magnified views of (a) and (c), respectively. The shear band**  
304 **widths are indicated in the figures. The white dashed line represents the boundary between the gabbro block**  
305 **and brucite gouge.**

306

307



308 **4. Discussion**

309 **4.1. Mechanical weakness of a small amount of brucite**

310 Based on the microstructural observations in Sect. 3.2, the boundary shear is smooth, filling the  
311 rough surface of the gabbro block as a “fault mirror” (Siman-Tov et al., 2013). The brucite particles are  
312 aligned along the boundary shear, indicating that the deformation within the narrow shear band is  
313 responsible for most of the deformation of the gouge during the steady state. In addition, the constant gouge  
314 thickness during the steady state suggests that the gouge deformation occurs parallel to the shear direction,  
315 confirming that the shear deformation within the gouge occurs within the shear band.

316 Because previous studies showed that friction with a smooth slip surface reduces the friction  
317 coefficients (Anthony and Marone, 2005), the smooth boundary shear observed in this study would reduce  
318 the friction coefficient with increasing shear displacement (Haines et al., 2013). In addition, the slip  
319 between the basal planes of sheet-structure minerals also plays an important role for weak friction because  
320 the friction between single crystals of sheet-structure minerals has a lower friction coefficient than that of  
321 powdered samples (Kawai et al., 2015; Niemeijer, 2018; Okamoto et al., 2019). Based on the observed  
322 alignment of the basal plane of brucite within the shear band, the friction between brucite crystals might  
323 enhance the weak friction of brucite. Because the preferred planes of nanoparticles tend to be aligned even  
324 when the velocity is low (Verberne et al., 2013, 2014b), nanoparticles could indirectly contribute to the  
325 slip-weakening behavior. Based on these phenomena, we conclude that the mechanical weakness of brucite  
326 observed in this study is derived from the smooth boundary shear of fine brucite particles and alignment of  
327 the basal plane of brucite parallel to the boundary shear.

328 The results of several previous experimental studies showed that the friction coefficient of a  
329 mixture of strong and weak materials inversely correlates with the volume of the weak materials (Giorgetti  
330 et al., 2015; Logan and Rauenzahn, 1987; Moore and Lockner, 2011; Niemeijer and Spiers, 2007;  
331 Shimamoto and Logan, 1981; Takahashi et al., 2007; Tembe et al., 2010). Based on the maximum amount



332 of brucite in serpentinite, that is ~20 vol. % (Kawahara et al., 2016; Moore et al., 2001), the expected  
333 friction coefficient of the antigorite–brucite mixture is 0.53, assuming a simple linear mixing law between  
334 the wet friction coefficients of 0.6 for antigorite and 0.26 for brucite. This value is not small, but the bulk  
335 friction coefficient of the mixture will decrease if weak brucite crystals are interconnected with each other.  
336 The microstructural observations showed that the shear band is less than 50  $\mu\text{m}$  wide (Sect. 3.2.2; Fig. 7);  
337 therefore, a narrow network of brucite can weaken the bulk strength. The results of a recent petrographic  
338 study of a hydrated paleo-mantle wedge revealed brucite thin films parallel to antigorite particles,  
339 suggesting the significant role of brucite in the development of the sheared structure of the antigorite–  
340 brucite assemblage in the hydrated mantle wedge (Mizukami et al., 2014). Because the maximum width of  
341 the brucite film in the antigorite–brucite assemblage is several hundred micrometers (Kawahara et al., 2016;  
342 Mizukami et al., 2014), that is, larger than 50  $\mu\text{m}$ , brucite has the potential to drastically weaken the bulk  
343 strength of serpentinite.

344

#### 345 4.2. Application to the mantle wedge condition

346 To interpret the effect of brucite on the seismic activities in the mantle wedge, the effect of  
347 temperature should be considered because all our experiments were conducted under room-temperature  
348 conditions. According to previous experiments under hydrothermal conditions in which the temperature  
349 was varied, the friction coefficient the  $a - b$  values decrease with increasing temperature (Moore et al.,  
350 2001; Moore and Lockner, 2007). Because a nearly neutral  $a - b$  value was observed at an effective  
351 normal stress of 150 MPa and temperature of 340  $^{\circ}\text{C}$  (Moore et al., 2001), brucite shows an unstable  
352 behavior under a wide range of pressure–temperature conditions, especially at low effective normal stress.  
353 Based on the estimated frictional properties of brucite under the mantle wedge condition, we compared  
354 brucite to other mineral phases to interpret the earthquake processes within the mantle wedge (Fig. 8).



355 In the mantle wedge, ultramafic minerals, such as olivine, transform into serpentine minerals,  
356 such as antigorite, talc, and brucite, due to hydration. In cold subduction zones, such as beneath NE Japan,  
357 likely containing brucite under the pressure–temperature conditions of the mantle wedge, the stable mineral  
358 assemblages are lizardite-brucite (Liz–Brc) at depths shallower than 50 km or antigorite–brucite (Atg–Brc)  
359 assemblage under deeper and warmer conditions (Peacock and Hyndman, 1999). Previous experimental  
360 studies on antigorite suggested potential seismic activities due to the unstable frictional behavior of  
361 antigorite at high temperatures above 450 °C (Okazaki and Katayama, 2015; Takahashi et al., 2011) at  
362 which crustal (granitic) rock shows stable friction (Fig. 8), whose friction coefficient (0.5–0.7) is not as low  
363 as that of brucite (Fig. 8). Although, lizardite, which destabilizes at ~200 °C, potentially shows an unstable  
364 behavior at low temperature (Moore et al., 1997), its friction coefficient is 0.4–0.5, which is lower than that  
365 of antigorite but higher than that of brucite (Fig. 8). Therefore, antigorite and lizardite are not preferably  
366 deformed if other weaker minerals, such as brucite, are present.

367 Another candidate of such a weak mineral stable under mantle wedge conditions is talc. Talc has  
368 a low friction coefficient of 0.1–0.2 at low to high temperatures (Fig. 8); therefore, it might contribute to  
369 the creep behavior of the San Andreas fault (Moore and Lockner, 2008) or weaken the slab–mantle interface  
370 (Hirauchi et al., 2013; Hyndman and Peacock, 2003). However, because talc has a stable frictional behavior  
371 at any temperature, leading to aseismic creep (Moore and Lockner, 2008; Sánchez-Roa et al., 2017), it  
372 cannot nucleate earthquakes. Considering the occurrence of talc in the mantle wedge, talc is stable at when  
373 high Si concentrations and temperature, whereas the mineral assemblage consists of brucite and antigorite  
374 when the Si content and temperature are low (Peacock and Hyndman, 1999). Talc was not widely observed  
375 in the paleo-mantle wedge exposed in the Shiraga body, central Shikoku, Japan, with the temperature–  
376 pressure condition where the antigorite–brucite system is stable (Kawahara et al., 2016; Mizukami et al.,  
377 2014). Although only antigorite stably exists in the antigorite–brucite stability field when the Si content is  
378 high, brucite is widely distributed in the Shiraga body (~10–15 %), suggesting low Si metasomatism in the



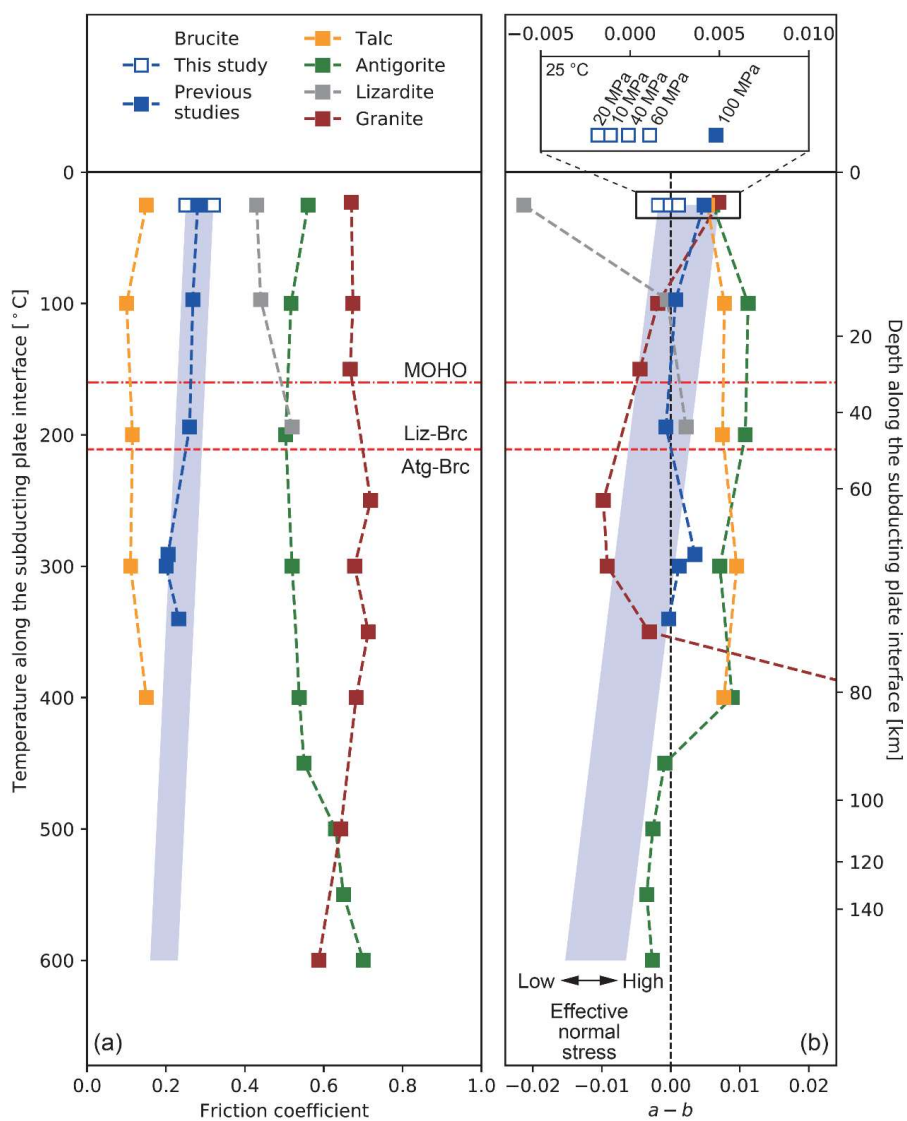
379 shallow hydrated mantle wedge (Kawahara et al., 2016). Hence, brucite can stably exist within the mantle  
380 wedge rather than talc. The distribution of brucite is associated with deformation and the brucite volume is  
381 high enough to weaken the bulk strength as discussed in Sect. 4.1; therefore, brucite might be a key mineral  
382 controlling the seismic activities in the shallow hydrated mantle wedge because brucite is the only mineral  
383 that has weak, unstable frictional characteristics under a wide range of temperature–pressure conditions  
384 (Fig. 8).

385           The results of recent seismological studies showed that the plate interfaces in the shallow mantle  
386 wedge have a nearly lithostatic pore pressure due to slab-derived water at various subduction zones such as  
387 SE Japan, Cascadia, Central Mexico, and Hikurangi (Audet et al., 2009; Audet and Kim, 2016; Eberhart-  
388 Phillips and Reyners, 2012; Matsubara et al., 2009; Shelly et al., 2006; Song and Kim, 2012). Such low  
389 effective normal stress conditions are conducive for brittle deformation rather than ductile behavior (French  
390 and Condit, 2019; Gao and Wang, 2017). Slow earthquakes in the mantle wedge of various subduction  
391 zones (Audet and Kim, 2016; Obara and Kato, 2016) might be induced by the low effective normal stress  
392 because low effective normal stress conditions are conducive for the nucleation of slow earthquake (Liu  
393 and Rice, 2007, 2009; Rubin, 2008; Segall et al., 2010). As  $a - b$  value of brucite decreases with  
394 decreasing effective normal stress, brucite at low effective normal stress possibly causes the nucleation of  
395 slow earthquakes in the mantle wedge. Notably, the possible presence of talc or brucite-free antigorite due  
396 to high Si content in the vicinity of the slab–mantle interface (Hirauchi et al., 2013; Peacock and Hyndman,  
397 1999) might affect the partitioning of deformation (French and Condit, 2019) and the contribution of brucite  
398 to the deformation. In addition, the linkage between high pore fluid pressure and the effective normal stress  
399 is still debated (Hirth and Beeler, 2015; Noda and Takahashi, 2016); therefore, experiments under  
400 hydrothermal conditions with high confining pressure and high pore fluid pressure must be conducted in  
401 the future.

402



403



404

405 **Figure 8: Friction coefficients (a) and velocity dependences (b) of brucite (this study; Moore et al., 2001), talc**  
 406 **(Moore and Lockner, 2008), antigorite (Okazaki and Katayama, 2015; Takahashi et al., 2011), lizardite (Moore**  
 407 **et al., 1997), and granite (Blanpied et al., 1998). The vertical axes are identical to the temperature gradient along**  
 408 **the subduction interface in NE Japan (Peacock and Wang, 1999). The red chain horizontal line represents the**  
 409 **typical depth of the MOHO. The red dotted horizontal line represents the phase boundary between lizardite–**



410 brucite (Liz–Brc) and antigorite–brucite (Atg–Brc; Peacock and Hyndman, 1999). The blue shaded areas are  
411 the estimated frictional characteristics extrapolated from experimental results. With the decrease in the effective  
412 normal stress, the  $a - b$  value decreases, as indicated by the arrow. This trend was confirmed at room  
413 temperature, as shown in the inset at the top of (b) and Fig. 4.

414

## 415 6. Conclusions

416 In this study, the influence of effective normal stress on the frictional characteristics of brucite  
417 was experimentally determined under both dry and water-saturated (wet) conditions at room temperature.  
418 The steady-state friction coefficients of brucite are 0.40 and 0.26 in the dry and wet cases, respectively,  
419 independently of the applied normal stress, while the peak friction coefficients are inversely correlated with  
420 the applied normal stress. In all dry experiments, velocity-weakening or stick-slip behavior was observed  
421 at every normal stress. In the wet experiments, velocity-weakening, -neutral, and -strengthening behaviors  
422 were observed at normal stresses of 10 and 20, 40, and 60 MPa, respectively. Combining with the previously  
423 reported temperature effect, this result suggests that brucite is weak and unstable under a wide temperature–  
424 pressure condition. The microstructural observations reveal that the low friction coefficient and slip  
425 weakening from the peak to steady-state friction coefficient are due to the smooth boundary shear and basal  
426 plane orientation parallel to the boundary shear. Because the deformation is concentrated within a narrow  
427 shear band with a width less than 50  $\mu\text{m}$ , a small amount of brucite can weaken the bulk strength of the  
428 antigorite–brucite assemblage. Compared to other serpentinite minerals, brucite is the only mineral that  
429 shows both low friction coefficient and velocity-weakening behavior. Hence, we conclude that weak,  
430 unstable brucite contributes to the nucleation of slow earthquake in the shallow hydrated mantle wedge.

431

432 **Table 1. Summary of the experimental conditions and results.**

---

Friction coefficient	$a - b$
----------------------	---------

---





Experiment	Condition	Normal stress	Final shear displacement	Peak value	Steady state (10 mm)	Steady state (20 mm)	Upsteps <sup>a</sup>	Downsteps <sup>a</sup>
HTB550	Dry	20 MPa	18 mm	0.67	0.36	0.35 <sup>b</sup>	N/A	N/A
HTB575	Dry	20 MPa	20 mm	0.68	0.46	0.44	-0.0047(3)	-0.0048(2)
HTB580	Dry	10 MPa	20 mm	0.77	0.49	0.45	-0.0024(4)	-0.0014(3)
ND1	Dry	20 MPa	0 mm	N/A	N/A	N/A	N/A	N/A
HTB593	Dry	20 MPa	1.5 mm <sup>c</sup>	N/A	N/A	N/A	N/A	N/A
HTB595	Dry	20 MPa	2.0 mm <sup>d</sup>	0.60	N/A	N/A	N/A	N/A
HTB598	Dry	20 MPa	20 mm	0.61	0.41	0.39	-0.0010(2)	-0.0009(2)
HTB601	Dry	20 MPa	10 mm	0.65	0.42	N/A	N/A	N/A
HTB641	Dry	40 MPa	20 mm	0.51	0.41	0.395	Negative (Stick-slip)	Negative (Stick-slip)
HTB642	Dry	60 MPa	20 mm	0.50	0.40	0.39	Negative (Stick-slip)	Negative (Stick-slip)
HTB734	Wet	20 MPa	20 mm	0.35	0.28	0.25	-0.0011(2)	-0.0018(1)
HTB735	Wet	20 MPa	10 mm	0.37	0.29	N/A	N/A	N/A
HTB736	Wet	20 MPa	1.2 mm <sup>c</sup>	N/A	N/A	N/A	N/A	N/A



HTB737	Wet	10 MPa	20 mm	0.39	0.32	0.31	-	-0.0011(2)
							0.0010(3)	)
HTB738	Wet	20 MPa	1.8 mm <sup>d</sup>	0.34	N/A	N/A	N/A	N/A
HTB739	Wet	40 MPa	20 mm	0.29	0.26	0.24	0.0001(2)	-0.0001(1)
							)	
HTB741	Wet	60 MPa	20 mm	0.33	0.25	0.25	0.0012(1)	0.0011(1)
							)	

*Note.* <sup>a</sup>All parameters ( $a$ ,  $b$ , and  $d_c$ ) used for the velocity step tests are listed in Table S1. <sup>b</sup>Value at the shear displacement of 18 mm. <sup>c</sup>Shear loading was stopped before the peak friction coefficient was reached. <sup>d</sup>Shear loading was stopped shortly after the peak friction coefficient was reached.

433

434

435

#### 436 **Data availability**

437 The results of all experimental data are available in the Supporting Information.

438

#### 439 **Author contributions**

440 H.O. conceptualized this study. H.O. and I.K. conducted the experiments. H.O. and H.S.

441 conducted analyses before experiments. H.O. carried out the formal analyses and microstructural analyses.

442 H.O. prepared the original manuscript, which was reviewed and edited by all coauthors. K.K. was the

443 supervisor. I.K., H.S., and K.K. designed the research project.

444



445 **Competing interests**

446 The authors declare that they have no conflict of interest.

447

448 **Acknowledgement**

449 We thank Y. Noda and R. Fujioka for the experiments, H. Ishisako for the preparation of thin  
450 sections, and A. Yamaguchi and N. Ogawa for SEM observations. This research was supported by  
451 KAKENHI grants (JP20J20413, JP20H00200, JP15H02147), and the Cooperative Program (No. 114,  
452 2019) of the Atmosphere and Ocean Research Institute, University of Tokyo. H.O. is supported by JSPS  
453 and FMSP as a research fellow.

454

455 **References**

456 Anthony, J. L. and Marone, C.: Influence of particle characteristics on granular friction, *J. Geophys. Res.*,  
457 110, B08409, <https://doi.org/10.1029/2004JB003399>, 2005.

458 Audet, P. and Kim, Y.: Teleseismic constraints on the geological environment of deep episodic slow  
459 earthquakes in subduction zone forearcs: A review, *Tectonophysics*, 670, 1–15,  
460 <https://doi.org/10.1016/j.tecto.2016.01.005>, 2016.

461 Audet, P., Bostock, M. G., Christensen, N. I. and Peacock, S. M.: Seismic evidence for overpressured  
462 subducted oceanic crust and megathrust fault sealing, *Nature*, 457, 76–78,  
463 <https://doi.org/10.1038/nature07650>, 2009.

464 Berman, H.: Fibrous brucite from Quebec, *Am. Mineral.*, 17, 313–316, 1932.

465 Bhattacharya, P., Rubin, A. M., Bayart, E., Savage, H. M. and Marone, C.: Critical evaluation of state  
466 evolution laws in rate and state friction: Fitting large velocity steps in simulated fault gouge with time-,



- 467 slip-, and stress-dependent constitutive laws, *J. Geophys. Res. Solid Earth*, 120, 6365–6385,  
468 <https://doi.org/10.1002/2015JB012437>, 2015.
- 469 Bhattacharya, P., Rubin, A. M. and Beeler, N. M.: Does fault strengthening in laboratory rock friction  
470 experiments really depend primarily upon time and not slip?, *J. Geophys. Res. Solid Earth*, 122, 6389–  
471 6430, <https://doi.org/10.1002/2017JB013936>, 2017.
- 472 Blanpied, M. L., Marone, C. J., Lockner, D. A., Byerlee, J. D. and King, D. P.: Quantitative measure of  
473 the variation in fault rheology due to fluid-rock interactions, *J. Geophys. Res. Solid Earth*, 103, 9691–  
474 9712, <https://doi.org/10.1029/98JB00162>, 1998.
- 475 Collettini, C., Viti, C., Smith, S. A. F. and Holdsworth, R. E.: Development of interconnected talc  
476 networks and weakening of continental low-angle normal faults, *Geology*, 37, 567–570,  
477 <https://doi.org/10.1130/G25645A.1>, 2009.
- 478 D’Antonio, M. and Kristensen, M. B.: Serpentine and brucite of ultramafic clasts from the South  
479 Chamorro Seamount (Ocean Drilling Program Leg 195, Site 1200): inferences for the serpentinization of  
480 the Mariana forearc mantle, *Mineral. Mag.*, 68, 887–904, <https://doi.org/10.1180/0026461046860229>,  
481 2004.
- 482 Deer, W. A., Howie, R. A. and Zussman, J. (Eds.): An introduction to the rock-forming minerals, 3rd ed.,  
483 Mineralogical Society, London, United Kingdom, 2013.
- 484 Dieterich, J. H.: Modeling of rock friction: 1. Experimental results and constitutive equations, *J. Geophys.*  
485 *Res.*, 84, 2161, <https://doi.org/10.1029/JB084iB05p02161>, 1979.
- 486 Eberhart-Phillips, D. and Reyners, M.: Imaging the Hikurangi Plate interface region, with improved local-  
487 earthquake tomography, *Geophys. J. Int.*, 190, 1221–1242, <https://doi.org/10.1111/j.1365->  
488 [246X.2012.05553.x](https://doi.org/10.1111/j.1365-246X.2012.05553.x), 2012.
- 489 Evans, B. W., Hattori, K. and Baronnet, A.: Serpentinite: What, Why, Where?, *Elements*, 9, 99–106,  
490 <https://doi.org/10.2113/gselements.9.2.99>, 2013.



- 491 French, M. E. and Condit, C. B.: Slip partitioning along an idealized subduction plate boundary at deep  
492 slow slip conditions, *Earth Planet. Sci. Lett.*, 528, 115828, <https://doi.org/10.1016/j.epsl.2019.115828>,  
493 2019.
- 494 Gao, X. and Wang, K.: Rheological separation of the megathrust seismogenic zone and episodic tremor  
495 and slip, *Nature*, 543, 416–419, <https://doi.org/10.1038/nature21389>, 2017.
- 496 Giorgetti, C., Carpenter, B. M. and Collettini, C.: Frictional behavior of talc-calcite mixtures, *J. Geophys.*  
497 *Res. Solid Earth*, 120, 6614–6633, <https://doi.org/10.1002/2015JB011970>, 2015.
- 498 Guillot, S., Schwartz, S., Reynard, B., Agard, P. and Prigent, C.: Tectonic significance of serpentinites,  
499 *Tectonophysics*, 646, 1–19, <https://doi.org/10.1016/j.tecto.2015.01.020>, 2015.
- 500 Haines, S. H., Kaproth, B., Marone, C., Saffer, D. M. and van der Pluijm, B. A.: Shear zones in clay-rich  
501 fault gouge: A laboratory study of fabric development and evolution, *J. Struct. Geol.*, 51, 206–225,  
502 <https://doi.org/10.1016/j.jsg.2013.01.002>, 2013.
- 503 Hirauchi, K., den Hartog, S. A. M. and Spiers, C. J.: Weakening of the slab–mantle wedge interface  
504 induced by metasomatic growth of talc, *Geology*, 41, 75–78, <https://doi.org/10.1130/G33552.1>, 2013.
- 505 Hirth, G. and Beeler, N. M.: The role of fluid pressure on frictional behavior at the base of the  
506 seismogenic zone, *Geology*, 43, 223–226, <https://doi.org/10.1130/G36361.1>, 2015.
- 507 Hirth, G. and Guillot, S.: Rheology and tectonic significance of serpentinite, *Elements*, 9, 107–113,  
508 <https://doi.org/10.2113/gselements.9.2.107>, 2013.
- 509 Horn, H. M. and Deere, D. U.: Frictional characteristics of minerals, *Géotechnique*, 12, 319–335,  
510 <https://doi.org/10.1680/geot.1962.12.4.319>, 1962.
- 511 Hostetler, P. B., Coleman, R. G., Mumpton, F. A. and Evans, B. W.: Brucite in Alpine Serpentinites, *Am.*  
512 *Mineral.*, 51, 75–98, 1966.
- 513 Hyndman, R. D. and Peacock, S. M.: Serpentinization of the forearc mantle, *Earth Planet. Sci. Lett.*, 212,  
514 417–432, [https://doi.org/10.1016/S0012-821X\(03\)00263-2](https://doi.org/10.1016/S0012-821X(03)00263-2), 2003.



515 Kawahara, H., Endo, S., Wallis, S. R., Nagaya, T., Mori, H. and Asahara, Y.: Brucite as an important  
516 phase of the shallow mantle wedge: Evidence from the Shiraga unit of the Sanbagawa subduction zone,  
517 SW Japan, *Lithos*, 254–255, 53–66, <https://doi.org/10.1016/j.lithos.2016.02.022>, 2016.

518 Kawai, K., Sakuma, H., Katayama, I. and Tamura, K.: Frictional characteristics of single and  
519 polycrystalline muscovite and influence of fluid chemistry, *J. Geophys. Res. Solid Earth*, 120, 6209–  
520 6218, <https://doi.org/10.1002/2015JB012286>, 2015.

521 Liu, Y. and Rice, J. R.: Spontaneous and triggered aseismic deformation transients in a subduction fault  
522 model, *J. Geophys. Res.*, 112, B09404, <https://doi.org/10.1029/2007JB004930>, 2007.

523 Liu, Y. and Rice, J. R.: Slow slip predictions based on granite and gabbro friction data compared to GPS  
524 measurements in northern Cascadia, *J. Geophys. Res. Solid Earth*, 114, 1–19,  
525 <https://doi.org/10.1029/2008JB006142>, 2009.

526 Logan, J. M. and Rauenzahn, K. A.: Frictional dependence of gouge mixtures of quartz and  
527 montmorillonite on velocity, composition and fabric, *Tectonophysics*, 144, 87–108,  
528 [https://doi.org/10.1016/0040-1951\(87\)90010-2](https://doi.org/10.1016/0040-1951(87)90010-2), 1987.

529 Logan, J. M., Dengo, C. A., Higgs, N. G. and Wang, Z. Z.: Fabrics of experimental fault zones: Their  
530 development and relationship to mechanical behavior, in: *Fault Mechanics and Transport Properties of*  
531 *Rocks*, edited by Evans, B. and Wong, T.F., Elsevier, 33–67, 1992.

532 Marone, C.: Laboratory-derived friction laws and their application to seismic faulting, *Annu. Rev. Earth*  
533 *Planet. Sci.*, 26, 643–696, <https://doi.org/10.1146/annurev.earth.26.1.643>, 1998.

534 Matsubara, M., Obara, K. and Kasahara, K.: High-VP/VS zone accompanying non-volcanic tremors and  
535 slow-slip events beneath southwestern Japan, *Tectonophysics*, 472, 6–17,  
536 <https://doi.org/10.1016/j.tecto.2008.06.013>, 2009.



- 537 Mizukami, T., Yokoyama, H., Hiramatsu, Y., Arai, S., Kawahara, H., Nagaya, T. and Wallis, S. R.: Two  
538 types of antigorite serpentinite controlling heterogeneous slow-slip behaviours of slab–mantle interface,  
539 Earth. Planet. Sci. Lett., 401, 148–158, <https://doi.org/10.1016/j.epsl.2014.06.009>, 2014.
- 540 Moore, D. E. and Lockner, D. A.: Crystallographic controls on the frictional behavior of dry and water-  
541 saturated sheet structure minerals, J. Geophys. Res., 109, B03401, <https://doi.org/10.1029/2003JB002582>,  
542 2004.
- 543 Moore, D. E. and Lockner, D. A.: Comparative deformation behavior of minerals in serpentinitized  
544 ultramafic rock: Application to the slab-mantle interface in subduction zones, International Geology  
545 Review, 49, 401–415, <https://doi.org/10.2747/0020-6814.49.5.401>, 2007.
- 546 Moore, D. E. and Lockner, D. A.: Talc friction in the temperature range 25°–400 °C: Relevance for fault-  
547 zone weakening, Tectonophysics, 449, 120–132, <https://doi.org/10.1016/j.tecto.2007.11.039>, 2008.
- 548 Moore, D. E. and Lockner, D. A.: Frictional strengths of talc-serpentine and talc-quartz mixtures, J.  
549 Geophys. Res., 116, B01403, <https://doi.org/10.1029/2010JB007881>, 2011.
- 550 Moore, D. E., Lockner, D. A., Ma, S., Summers, R. and Byerlee, J. D.: Strengths of serpentinite gouges at  
551 elevated temperatures, J. Geophys. Res. Solid Earth, 102, 14787–14801,  
552 <https://doi.org/10.1029/97JB00995>, 1997.
- 553 Moore, D. E., Lockner, D. A., Iwata, K., Tanaka, H. and Byerlee, J. D.: How brucite may affect the  
554 frictional properties of serpentinite, USGS Open-File Report, 1–14, 2001.
- 555 Morrow, C. A., Moore, D. E. and Lockner, D. A.: The effect of mineral bond strength and adsorbed water  
556 on fault gouge frictional strength, Geophys. Res. Lett., 27, 815–818,  
557 <https://doi.org/10.1029/1999GL008401>, 2000.
- 558 Niemeijer, A. R.: Velocity-dependent slip weakening by the combined operation of pressure solution and  
559 foliation development, Scientific Reports, 8, 4724, <https://doi.org/10.1038/s41598-018-22889-3>, 2018.



- 560 Niemeijer, A. R. and Spiers, C. J.: A microphysical model for strong velocity weakening in phyllosilicate-  
561 bearing fault gouges, *J. Geophys. Res.*, 112, B10405, <https://doi.org/10.1029/2007JB005008>, 2007.
- 562 Noda, H. and Shimamoto, T.: Constitutive properties of clayey fault gouge from the Hanaore fault zone,  
563 southwest Japan, *J. Geophys. Res.*, 114, B04409, <https://doi.org/10.1029/2008JB005683>, 2009.
- 564 Noda, H. and Takahashi, M.: The effective stress law at a brittle-plastic transition with a halite gouge  
565 layer, *Geophys. Res. Lett.*, 43, 1966–1972, <https://doi.org/10.1002/2015GL067544>, 2016.
- 566 Obara, K. and Kato, A.: Connecting slow earthquakes to huge earthquakes, *Science*, 353, 253–257,  
567 <https://doi.org/10.1126/science.aaf1512>, 2016.
- 568 Okamoto, A. S., Verberne, B. A., Niemeijer, A. R., Takahashi, M., Shimizu, I., Ueda, T. and Spiers, C. J.:  
569 Frictional properties of simulated chlorite gouge at hydrothermal conditions: Implications for subduction  
570 megathrusts, *J. Geophys. Res. Solid Earth*, 124, 4545–4565, <https://doi.org/10.1029/2018JB017205>,  
571 2019.
- 572 Okazaki, K. and Katayama, I.: Slow stick slip of antigorite serpentinite under hydrothermal conditions as  
573 a possible mechanism for slow earthquakes, *Geophys. Res. Lett.*, 42, 1099–1104,  
574 <https://doi.org/10.1002/2014GL062735>, 2015.
- 575 Okuda, H., Kawai, K. and Sakuma, H.: First-principles investigation of frictional characteristics of  
576 brucite: An application to its macroscopic frictional characteristics, *J. Geophys. Res. Solid Earth*, 124,  
577 10423–10443, <https://doi.org/10.1029/2019JB017740>, 2019.
- 578 Oleskevich, D. A., Hyndman, R. D. and Wang, K.: The updip and downdip limits to great subduction  
579 earthquakes: Thermal and structural models of Cascadia, south Alaska, SW Japan, and Chile, *J. Geophys.*  
580 *Res. Solid Earth*, 104, 14965–14991, <https://doi.org/10.1029/1999JB900060>, 1999.
- 581 Peacock, S. M. and Hyndman, R. D.: Hydrous minerals in the mantle wedge and the maximum depth of  
582 subduction thrust earthquakes, *Geophys. Res. Lett.*, 26, 2517–2520,  
583 <https://doi.org/10.1029/1999GL900558>, 1999.





- 584 Peacock, S. M. and Wang, K.: Seismic consequences of warm versus cool subduction metamorphism:  
585 Examples from southwest and northeast Japan, *Science*, 286, 937–939,  
586 <https://doi.org/10.1126/science.286.5441.937>, 1999.
- 587 Reinen, L. A., Weeks, J. D. and Tullis, T. E.: The frictional behavior of lizardite and antigorite  
588 serpentinites: Experiments, constitutive models, and implications for natural faults, *Pure Appl. Geophys.*,  
589 143, 317–358, <https://doi.org/10.1007/BF00874334>, 1994.
- 590 Rubín, A. M.: Episodic slow slip events and rate-and-state friction, *J. Geophys. Res.*, 113, B11414,  
591 <https://doi.org/10.1029/2008JB005642>, 2008.
- 592 Ruina, A. L.: Slip instability and state variable friction laws, *J. Geophys. Res. Solid Earth*, 88, 10359–  
593 10370, <https://doi.org/10.1029/JB088iB12p10359>, 1983.
- 594 Sánchez-Roa, C., Faulkner, D. R., Boulton, C., Jimenez-Millan, J. and Nieto, F.: How phyllosilicate  
595 mineral structure affects fault strength in Mg-rich fault systems, *Geophys. Res. Lett.*, 44, 5457–5467,  
596 <https://doi.org/10.1002/2017GL073055>, 2017.
- 597 Segall, P., Rubín, A. M., Bradley, A. M. and Rice, J. R.: Dilatant strengthening as a mechanism for slow  
598 slip events, *J. Geophys. Res.*, 115, B12305, <https://doi.org/10.1029/2010JB007449>, 2010.
- 599 Shelly, D. R., Beroza, G. C., Ide, S. and Nakamura, S.: Low-frequency earthquakes in Shikoku, Japan,  
600 and their relationship to episodic tremor and slip, *Nature*, 442, 188–191,  
601 <https://doi.org/10.1038/nature04931>, 2006.
- 602 Shimamoto, T. and Logan, J. M.: Effects of simulated clay gouges on the sliding behavior of Tennessee  
603 sandstone, *Tectonophysics*, 75, 243–255, [https://doi.org/10.1016/0040-1951\(81\)90276-6](https://doi.org/10.1016/0040-1951(81)90276-6), 1981.
- 604 Siman-Tov, S., Aharonov, E., Sagy, A. and Emmanuel, S.: Nanograins form carbonate fault mirrors,  
605 *Geology*, 41, 703–706, <https://doi.org/10.1130/G34087.1>, 2013.



606 Skarbek, R. M. and Savage, H. M.: RSFit3000: A MATLAB GUI-based program for determining rate  
607 and state frictional parameters from experimental data, *Geosphere*, 15, 1665–1676,  
608 <https://doi.org/10.1130/GES02122.1>, 2019.

609 Song, T.-R. A. and Kim, Y.: Localized seismic anisotropy associated with long-term slow-slip events  
610 beneath southern Mexico, *Geophys. Res. Lett.*, 39, L09308, <https://doi.org/10.1029/2012GL051324>,  
611 2012.

612 Takahashi, M., Mizoguchi, K., Kitamura, K. and Masuda, K.: Effects of clay content on the frictional  
613 strength and fluid transport property of faults, *J. Geophys. Res.*, 112, B08206,  
614 <https://doi.org/10.1029/2006JB004678>, 2007.

615 Takahashi, M., Uehara, S.-I., Mizoguchi, K., Shimizu, I., Okazaki, K. and Masuda, K.: On the transient  
616 response of serpentine (antigorite) gouge to stepwise changes in slip velocity under high-temperature  
617 conditions, *J. Geophys. Res.*, 116, B10405, <https://doi.org/10.1029/2010JB008062>, 2011.

618 Tembe, S., Lockner, D. A. and Wong, T.-F.: Effect of clay content and mineralogy on frictional sliding  
619 behavior of simulated gouges: Binary and ternary mixtures of quartz, illite, and montmorillonite, *J.*  
620 *Geophys. Res.*, 115, B03416, <https://doi.org/10.1029/2009JB006383>, 2010.

621 Tesei, T., Harbord, C. W. A., De Paola, N., Collettini, C. and Viti, C.: Friction of mineralogically  
622 controlled serpentinites and implications for fault weakness, *J. Geophys. Res. Solid Earth*, 123, 6976–  
623 6991, <https://doi.org/10.1029/2018JB016058>, 2018.

624 Verberne, B. A., De Bresser, J. H. P., Niemeijer, A. R., Spiers, C. J., de Winter, D. A. M. and Plümper,  
625 O.: Nanocrystalline slip zones in calcite fault gouge show intense crystallographic preferred orientation:  
626 Crystal plasticity at sub-seismic slip rates at 18–150 °C, *Geology*, 41, 863–866,  
627 <https://doi.org/10.1130/G34279.1>, 2013.



628 Verberne, B. A., Spiers, C. J., Niemeijer, A. R., De Bresser, J. H. P., de Winter, D. A. M. and Plümpner,  
629 O.: Frictional properties and microstructure of calcite-rich fault gouges sheared at sub-seismic sliding  
630 velocities, *Pure Appl. Geophys.*, 171, 2617–2640, <https://doi.org/10.1007/s00024-013-0760-0>, 2014a.  
631 Verberne, B. A., Plümpner, O., de Winter, D. A. M. and Spiers, C. J.: Superplastic nanofibrous slip zones  
632 control seismogenic fault friction, *Science*, 346, 1342–1344, <https://doi.org/10.1126/science.1259003>,  
633 2014b.  
634 Viti, C.: Exploring fault rocks at the nanoscale, *J. Struct. Geol.*, 33, 1715–1727,  
635 <https://doi.org/10.1016/j.jsg.2011.10.005>, 2011.  
636